PNAS RESEARCH ARTICLE | BIOPHYSICS AND COMPUTATIONAL BIOLOGY

Cilia-driven epithelial folding and unfolding in an early diverging animal

Charlotte M. Brannon[a] and Manu Prakash[a,b,c,d,1]

Affiliations are included on p. 10.

Edited by Brigid Hogan, Duke University Medical Center, Durham, NC; received July 8, 2025; accepted October 30, 2025

Multicellular organisms utilize epithelial folding to achieve remarkable three-dimensional forms. During embryonic development, stereotypical epithelial folds emerge from underlying active cellular and molecular processes including cell shape change and differential cell growth. However, the origin of epithelial folding in early animals and how folding may be harnessed in synthetic systems remain open questions. Here, we identify a modality of behavior-induced epithelial folding and unfolding arising from cilia–substrate adhesion and ciliary walking in the basal animal *Trichoplax adhaerens* (phylum Placozoa). We show that *T. adhaerens* is capable of exhibiting dynamic nonstereotyped folding states, providing a 3D perspective to an organism previously only characterized in its 2D state. We correlate these folding states to local substrate geometry, revealing that the animal conforms to available substrate surface area, promoting the maintenance of a folded state. Using 4D fluorescence light sheet microscopy, we characterize fold geometry, curvature evolution during unfolding, and the nonstereotypy of unfolding behavior. Through repeated unfolding trials, we reveal the robustness and timescales associated with unfolding behavior and employ scaling analysis and toy model simulations to establish how collective ciliary activity can robustly drive unfolding. In this way, despite lacking any folding–unfolding "pathway," transitions between folding and unfolding states emerge as a function of the animal's environment and motility. Our work reveals a remarkable behavior exhibited by a brainless, nerveless animal, and demonstrates the capacity for 3D–2D transitions in folding epithelial sheets using ciliary activity.

Placozoa | *Trichoplax adhaerens* | epithelial folding | cilia | active origami

Significance

Our findings unveil a unique epithelial folding–unfolding transition exhibited by the early diverging animal *Trichoplax adhaerens*. We demonstrate that *T. adhaerens* displays high-curvature body folding states as a function of substrate geometry, constituting a class of epithelial folding driven by dynamic substrate adhesion and distributed cellular activity. In contrast to the highly programmed folding processes in animal development, our study highlights an example of variable folding states arising from stochastic ciliary active-adhesion. These findings provide an example for the broad configuration space of unconstrained active thin-sheet folding, laying groundwork for future efforts to program thin-sheet folding in both living tissues and nonliving materials and establishing a model system for studying thin-sheet folding mechanics.

Epithelial folding is ubiquitous in animal embryogenesis (1–3). Detailed studies of model systems such as the *Drosophila* ventral furrow (4) have revealed key cellular and molecular processes that drive epithelial folding in development, including cellular shape change (5), apical constriction (6, 7), and differential cell growth (8, 9). These mechanisms, in combination with morphogenic regulation, enable the initiation of "stereotyped" (defined as predictable and invariant) folds in a spatiotemporally controlled fashion critical for the robust coordination of developmental processes such as neurulation and gastrulation (10). Deviations from normal folding in human development can lead to conditions such as polymicrogyria (11) and spina bifida (12).

Before the evolution of tightly controlled folding in development, what principles governed epithelial shape, form, and behavior? Folding and wrinkling are emergent properties of active soft materials (13, 14). Yet, how animal evolution constrained these processes in favor of programmed, stereotyped folding is unclear. The earliest physical constraints on epithelial folding and their consequences for the form and function of early animals have not been considered. Furthermore, the full scope of cellular and environmental mechanisms capable of guiding epithelial folding is not well understood. Just as simple multicellular organisms such as colonial choanoflagellates, ichthyosporeans, and volvox embryos have been harnessed to study the origins of morphing multicellular systems (15–17), new experimental systems are needed to study the constraints on epithelial folding in the context of the early evolution of animal form.

In this article, we present the identification of an epithelial folding and unfolding behavior driven by collective ciliary mechanics in the early diverging animal, *Trichoplax adhaerens* (phylum Placozoa) (Fig. 1*A* and Movie S1). Often described as the simplest extant animal in terms of morphology, this aneural and amuscular organism displays a sheet-like body plan with a ciliated ventral epithelium responsible for locomotion (19, 20) (Fig. 1*A*). While previous literature has primarily treated *T. adhaerens* as flat

Author contributions: C.M.B. and M.P. designed research; C.M.B. performed research; C.M.B. contributed new analytic tools and analyzed data in discussion with M.P.; and C.M.B. and M.P. wrote the paper.

The authors declare no competing interest.

This article is a PNAS Direct Submission.

[1] To whom correspondence may be addressed. Email: manup@stanford.edu.

This article contains supporting information online at https://www.pnas.org/lookup/suppl/doi:10.1073/pnas.2517741122/-/DCSupplemental.

Published December 16, 2025.

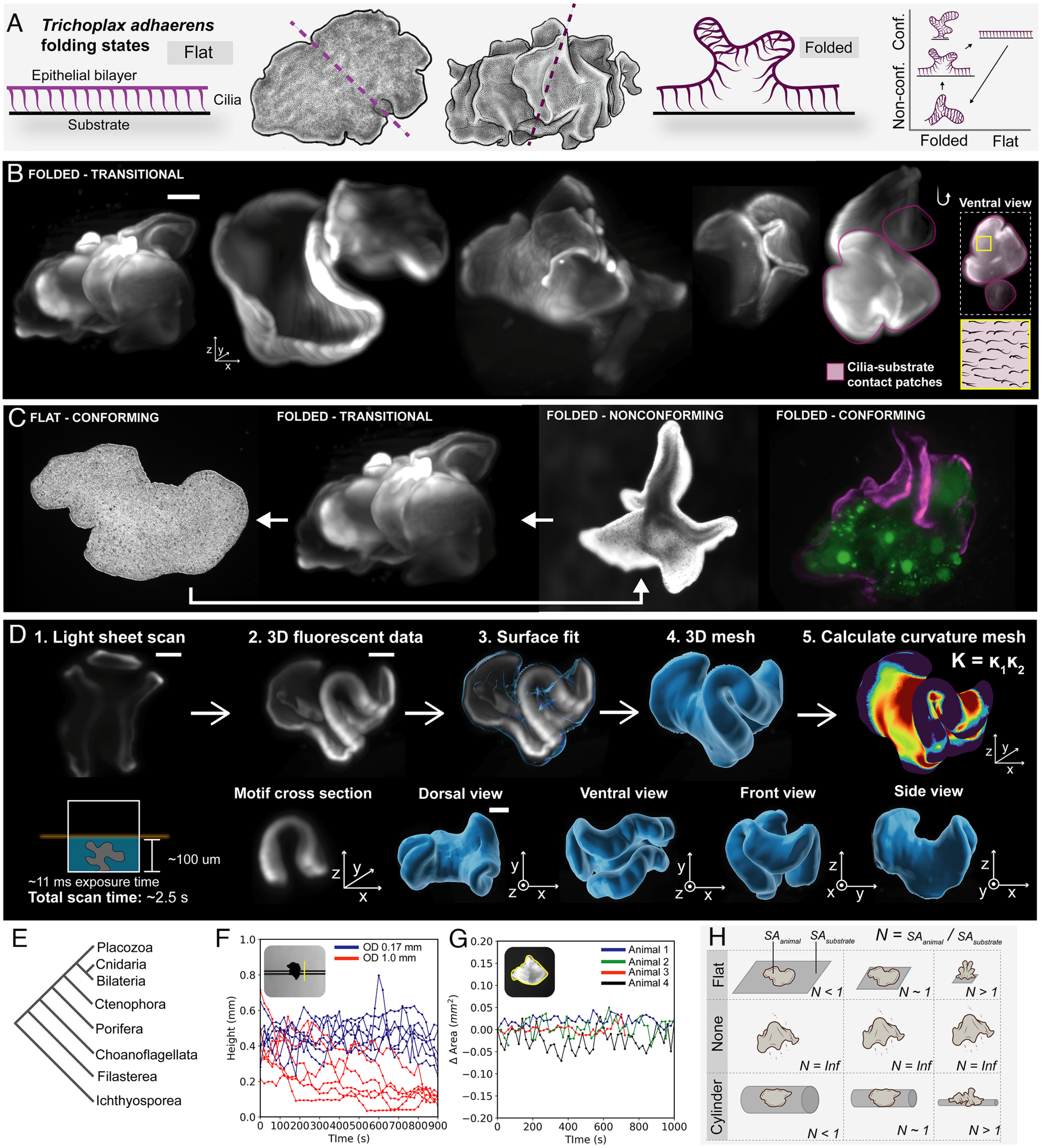

Fig. 1. *T. adhaerens* exhibits epithelial folding guided by substrate geometry. (*A*) *T. adhaerens* displays both flat and folded morphologies. These morphologies may be categorized as flat vs. folded and conforming vs. nonconforming to a substrate. (*B*) 3D light sheet scans of five different folded animals labeled with plasma membrane stain (*Materials and Methods*), perspective view. These animals are observed in the folded-transitional state undergoing unfolding behavior. *Inset* shows a ventral view, revealing distinct patches of the ciliated ventral epithelium that make contact with the substrate. (*C*) Categorization of *T. adhaerens* based on folding state and substrate interaction. Folded states emerge when a recently detached animal is in the process of conforming back to a flat substrate (folded-transitional); in the absence of a substrate (folded-nonconforming); and when conforming to a substrate with a lower surface area than that of the animal (folded-conforming). The transition from the folded-nonconforming state to the flat-conforming state via the folded-transitional state is termed unfolding behavior. (*D*) Workflow for extracting folding states from light sheet data. 3D datasets enable the complete description of the animal's folding state, along with identification of motifs and curvature analysis. (*E*) *T. adhaerens* phylogeny relative to other animal relatives (18). (*F*) Folding dynamics of *T. adhaerens* conforming to a thin glass capillary with an outer diameter of 0.17 mm (blue) and 1.0 mm (red). The low surface area of the 0.17 mm case leads to the maintenance of folds, while the 1.0 mm case provides sufficient surface area for the animal to reach the flat-conforming state. Each curve represents a different animal trial. Animal height on the capillary is used as a measure of folding, as indicated by the vertical yellow line in the *Inset* image. (*G*) In the absence of a rigid substrate (suspended in a water column), animals remain in the folded-nonconforming state. Animals at 0 s were folded, and visible animal area is used as a measure of folding, as indicated by the yellow outline in the *Inset* image. (*H*) Summary schematic illustrating how substrate geometry impacts folding state. When the ratio of animal to substrate surface area $N < 1$, the animal can attain the flat-conforming state. When $N > 1$, the animal stays in the folded-conforming state. [Scale bars: (*B*) 150 μm and (*D*) 100 μm.]

and pancake-like, here we reveal the folding states exhibited by the animal in the context of its environment (Fig. 1 *A*–*C*). We show that these states can arise as a function of local substrate geometry, demonstrating the importance of the environment in shaping the animal's morphology. Using a combination of whole-animal tracking microscopy and 4D light sheet fluorescence microscopy in live animals, we show that *T. adhaerens* exhibits active folding and unfolding behavior on fast timescales (seconds to minutes). This behavior is reversible and nonstereotyped, distinguishing it from epithelial folding processes in development. Via simple unfolding assays, we collect statistics to reveal the robustness of this folding–unfolding transition and leverage 4D datasets to identify common folding motifs. Finally, we employ scaling analysis and toy model simulations to show how the strength of substrate adhesion and collective ciliary activity encode emergent, robust active unfolding algorithms.

Results

Placozoan Folding and Substrate Geometry. By observing *T. adhaerens* in different substrate contexts, we identify four distinct morphological states of the animal (Fig. 1 *A*–*C*). (1) On a flat substrate, the animal displays a surface-conforming pancake-like 2D morphology characterized extensively in past literature ("flat-conforming" in Fig. 1*C*) (19–25). (2) The absence of a substrate leads to a dynamic yet folded 3D morphology ("folded-nonconforming" in Fig. 1*C*). Using vertical tracking microscopy (26), we imaged *T. adhaerens* in the absence of any rigid substrate falling in a water column under the influence of gravity, revealing the continued persistence of a folded state (Fig. 1*G* and Movie S2), indicating that attachment to a rigid substrate is necessary for the organism to transition to a flat state. Additionally, we regularly observe folded, detached animals in laboratory cultures, further supporting this intuition (*SI Appendix*, Fig. S1). (3) Detached animals reestablishing contact with a flat substrate remain temporarily folded until they can eventually flatten ("folded-transitional" in Fig. 1*C*; see also Fig. 1*B*). The transition from folded-nonconforming to flat-conforming via folded-transitional occurs regularly in laboratory culture conditions. We term this transition "unfolding behavior." (4) Finally, on irregular substrates, the animal displays a folded yet substrate-conforming state ("folded-conforming" in Fig. 1*C*). We investigated this folded-conforming state via unfolding trials on thin glass capillaries, revealing the animal's tendency to remain in an attached, dynamic folding state in the presence of low substrate area ($SA_{substrate}$) relative to the ventral surface area of a given animal (SA_{animal}) (Fig. 1*F* and Movie S3). These cases of attachment to irregular (nonflat) substrates exhibited by this ultrathin animal indicate a high adhesion, low bending energy regime (27). Accordingly, we identify a nondimensional number N which describes the ratio of the animal's ventral surface area to the available substrate surface area (Fig. 1*H*). When $N < 1$, a folded state is maintained, as the animal attempts to attach to a substrate with insufficient area. When $N > 1$, a folded animal will gradually return to a flattened state, as the ventral cilia interact with the substrate. This phenomenon is akin to area mismatches that occur in developing tissues, though without any tissue growth in this case (28). Interestingly, we observed a similar behavior occurring naturally in our cultures, where animals attach to and fold on globular algal clusters (sp. unknown), conforming to the irregular geometry of the cluster ("folded-conforming" in Fig. 1*C* and Movie S4). In this way, substrate geometry guides the folding morphotype of *T. adhaerens*, as substrate adhesion dominates over bending energy.

3D Structural Characterization of Folding States. Given these four morphological states, we focused our attention on unfolding behavior (transition from folded-nonconforming to flat-conforming via folded-transitional, Fig. 1 *B* and *C*). To determine how the animal achieves this transition, we first investigated the geometry of folding states over the course of unfolding. Previous physical studies focused on crumpled paper have relied on volumetric imaging techniques to establish the relationship between three-dimensional structure and folding/unfolding dynamics (29–32). In a similar vein, we performed 4D imaging (in live animals) and 3D confocal scans (in fixed animals) of membrane-labeled unfolding animals (Fig. 2 *A*–*C*, Movie S5, and *Materials and Methods*). In contrast to the relatively slow timescales associated with tissue folding in other systems such as animal embryos and bacterial biofilms, *T. adhaerens*' folds evolve on second timescales, presenting a unique challenge for 3D visualization. Low-exposure light sheet scans enabled the visualization of the animal's folding states over time (Fig. 1*D*).

From these data, it is apparent that folds are high-curvature, hierarchical structures, which display variable geometries (Fig. 2 *A*–*C* and Movie S5). Folds are distributed throughout the animal's body and do not leave a structural memory after being resolved (Fig. 2*A*). Furthermore, folding states are dynamic, exhibiting dramatic structural changes on the order of seconds (Fig. 2*A*). We fit smooth surfaces to these folded geometries and extracted local Gaussian curvature across the body (Fig. 2 *A* and *C*, Movie S6, and *Materials and Methods*), revealing the animal's ability to increase body curvature in the process of unfolding before eventually reaching a flat state. The nonmonotonicity of curvature evolution highlights the inherent frustration in the associated energy landscape for unfolding (Fig. 2*C*). Confocal scans of fixed folded animals revealed, in the most extreme cases, as few as three cells spanning the cusp of a fold (Fig. 2*B*). Additionally, we extracted an inner fold width of 5 to 10 μm, implying the presence of cilia–cilia contact within high-curvature folds (Fig. 2*D* and *SI Appendix*, Fig. S1) (20). In this way, folds establish domains of cilia–cilia contact, removing cilia from their interaction with the substrate. Moreover, the system is able to maintain and introduce high curvatures, pointing to the role of active processes in driving folding–unfolding dynamics.

Folding Motif Dynamics. Previous studies of epithelial folding in the context of animal morphogenesis have revealed distinct motifs such as furrows, ridges, branches, and loops (33). Although *T. adhaerens* folding states are not stereotyped, we identify specific folding motifs in our data, including 1) perimeter folds, 2) rucks, 3) hairpin folds, 4) balloon folds, 5) sealed folds, and 6) 2π twists (Fig. 3*A*) (34–37). This nonexhaustive but illustrative list of motifs provides a handle on *T. adhaerens* folding dynamics. Interestingly, each of the identified motifs (except for 2π twists) is biased toward negative ventral (positive dorsal) curvature, hinting at the role of adhesion between the ventral cilia and substrate in driving folding and unfolding processes. Tracking the time evolution of hairpin folds and rucks (Fig. 3*B*) reveals variable scaling between height and width of these motifs (Fig. 3 *F* and *G*). While ruck height scales with ruck width, hairpin folds change height without changing width, suggesting the presence of adhesive self-contact within the fold (Fig. 3 *F* and *G*). Additionally, extracting local cross-sectional curvature allows us

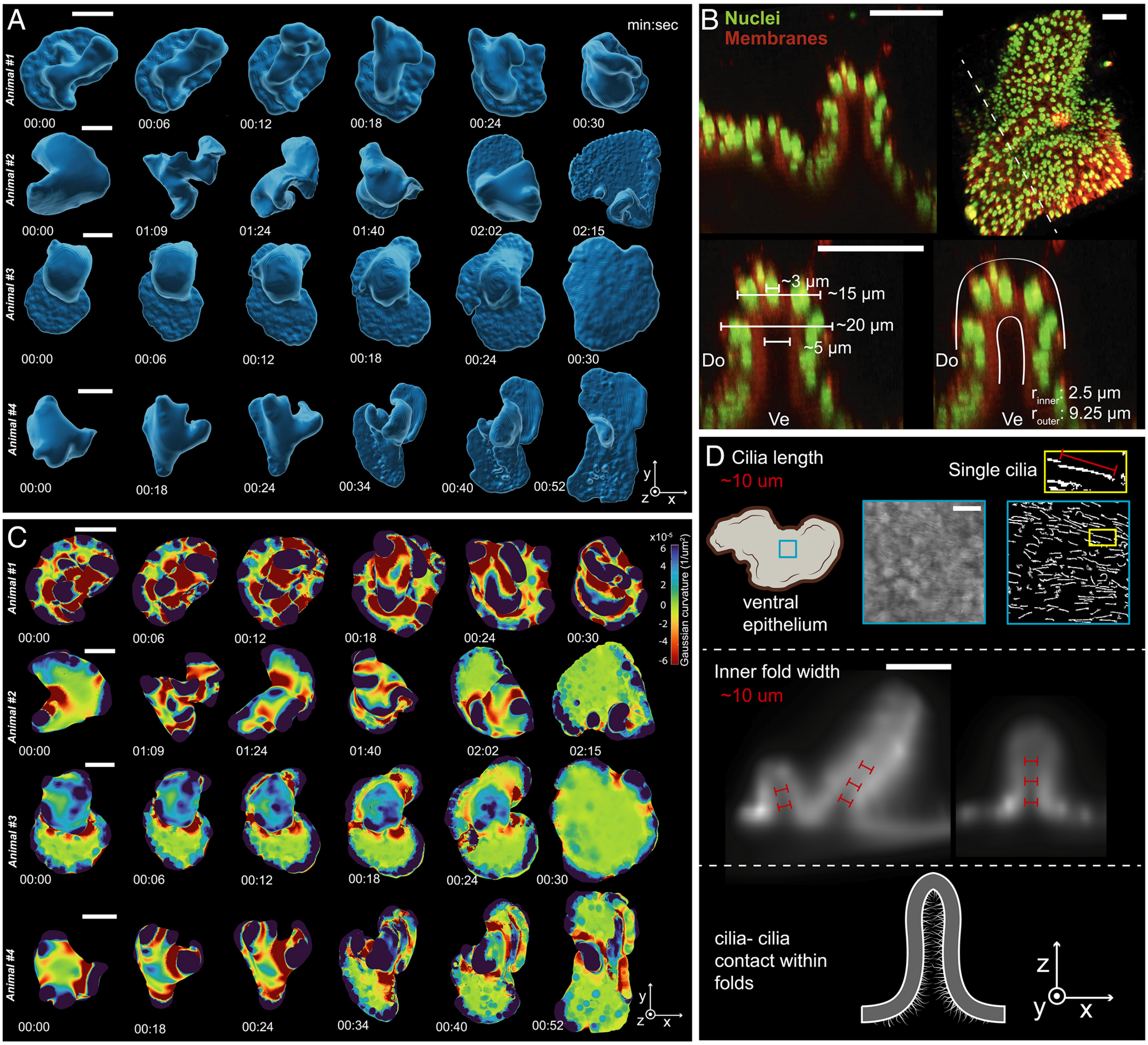

Fig. 2. Curvature evolution of unfolding behavior. (*A*) 4D light sheet imaging of unfolding behavior (transition from folded-nonconforming to flat-conforming via folded-transitional state, as defined in Fig. 1*C*) shown for four different animals. Dorsal view, surface meshes shown. The variety of initial folding states, unfolding trajectories, and emergent fold structures are apparent. (*B*) Cellular perspective within folds. Confocal scans of fixed folded animals labeled with Hoechst nucleic acid stain (green) and CellMask plasma membrane stain (red) reveal ~3 cells spanning the cusp of a high-curvature fold. (*C*) Extraction of local Gaussian curvature from surface meshes shown in (*A*) yields local curvature maps. Curvature evolution is nonmonotonic, which demonstrates the importance of activity in shaping the animal's folding state. (*D*) Extraction of ciliary length and inner fold width (both ~10 µm), indicating the presence of cilia–cilia contact within folds (*SI Appendix*, Fig. S1). [Scale bars: (*A* and *C*) 200 µm, (*B*) 20 µm, (*D*) 10 µm (*Top* row) and 100 µm (*Bottom* row).]

to quantify motif-specific curvature evolution (Fig. 3 *B*, *H*, and *I*). We find that rucks undergo gradual curvature removal, while hairpin folds maintain constant curvature until the moment they are removed (Fig. 3 *B*, *H*, and *I*). In this way, distinct folding motifs undergo unique geometric transformations as they are resolved.

We next consider the relationship between fold area and length. As can be seen in Fig. 3*D*, hairpin and perimeter folds display distinct crease lines on the ventral surface, which are observed to change in length over time as more material is absorbed into (or removed from) the fold. From the rough geometry of a growing perimeter fold, we show that the change in length should scale approximately as $(\sqrt{L^2 + \Delta A/\tan\theta}) - L$ and for a shrinking fold, $L - (\sqrt{L^2 - \Delta A/\tan\theta})$, where L is the length of the crease, ΔA is the change in fold area during a given time step, and θ is the maximum angle (based on sheet elasticity) the fold base can make with the substrate (Fig. 3 *D* and *E*, see *Materials and Methods* and *SI Appendix* for details). Notably, this behavior exhibits similar dynamics to contact line pinning in liquid droplets on surfaces, which only begin to expand in contact area upon reaching a critical angle set by the liquid and surface properties (38) (see *SI Appendix* for further discussion). Fitting the data in Fig. 3*J* to the above equations yields a predicted $\theta \approx 45°$, which is similar to that observed in our 3D data ($\theta \approx 42°$, Fig. 3 *D* and *J*).

Finally, we turn our attention to the 2π twist motif. We clearly observe variability in twist tightness within a single animal over the course of unfolding (Fig. 3 *C* and *K* and Movie S7). The tightest twist observed in our data is ~10 µm wide, on the order of a single dorsal epithelial cell diameter. Furthermore, time-lapse data revealed extensive twist mobility, analogous of topological

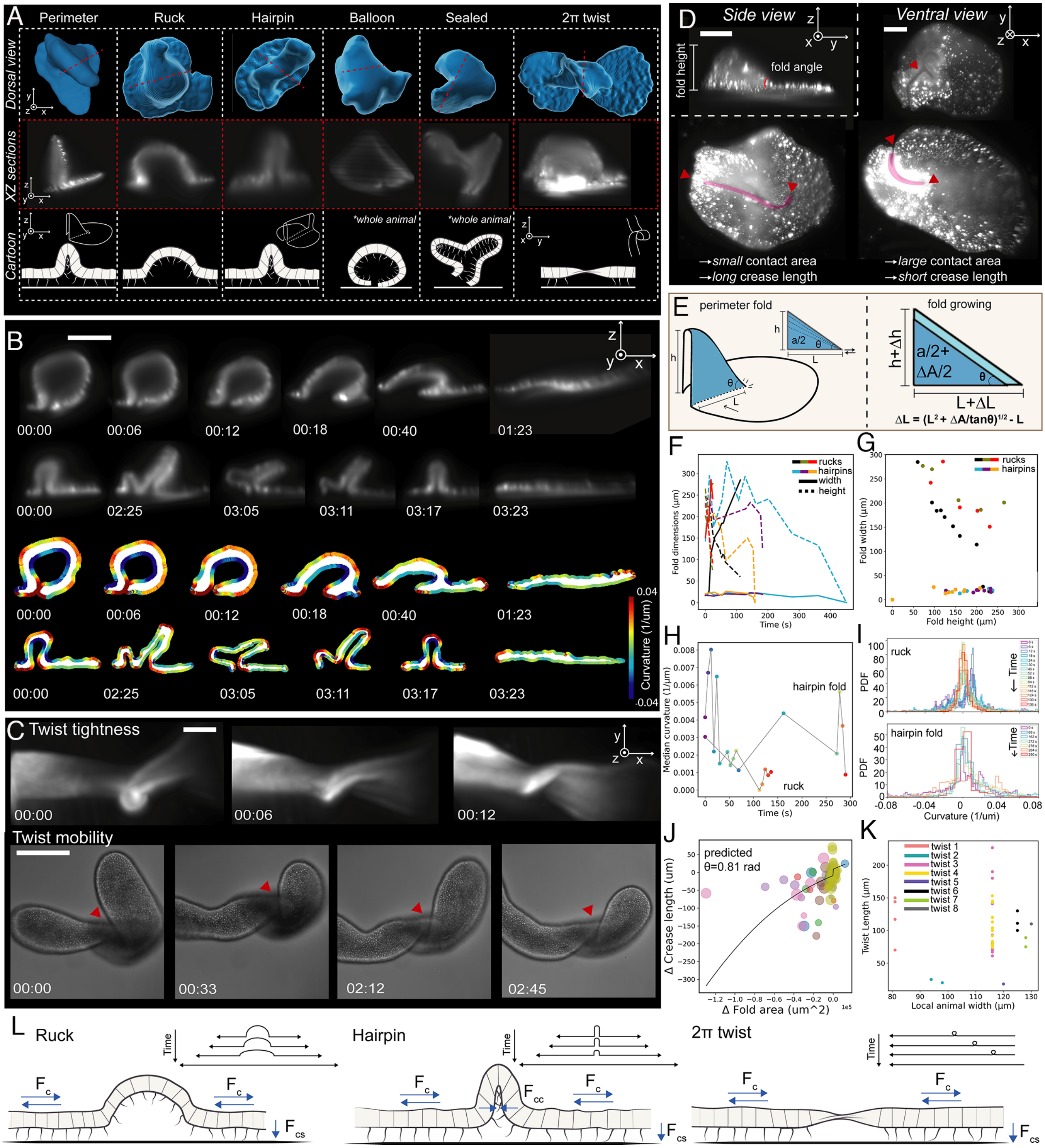

Fig. 3. Dynamics of 3D folding motifs. (*A*) Folding motifs include perimeter folds, rucks, hairpin folds, balloon folds, sealed folds, and 2π twists. Dorsal view (*Top* row), cross-sectional view (*Middle* row indicated by the red dotted line in the *Top* row), and cartoon schematic of each motif (*Bottom* row). Balloon and sealed motifs span the entire body, whereas perimeter, ruck, hairpin, and twist motifs are local. (*B*) cross-sectional time lapse imaging of individual ruck and hairpin folds with local curvature maps. These folds are observed to reduce in height locally, rather than being pushed out the edge of the body. (*C*) 2π twists display mobility and variation in tightness. Unlike folds, twists behave as point defects which must be removed from the edge of the body. (*D*) Visualization of a perimeter fold height and angle (i.e., the angle the fold base makes with the substrate). In the ventral view, crease lines (pink) are observed, which vary in length as material is added to or removed from the fold. (*E*) From a simple geometric representation of a perimeter fold, we estimate how crease length is expected to scale with fold area as folds grow and shrink in height. (*F*) Fold width and height time evolution for the ruck and fold shown in (*B*) and additional rucks and folds shown in *SI Appendix*, Fig. S1. (*G*) Fold width and height scaling. Hairpin folds (blue, orange, purple) exhibit constant fold width for variable heights, while ruck width scales with height (black, green, red). (*H*) Median curvature evolution for the ruck and fold shown in (*B*). While hairpin folds with self-contact exhibit relatively steady median curvature over time, rucks undergo gradual curvature reduction with removal. (*I*) Curvature evolution distributions for the ruck and fold shown in (*B*). (*J*) Change in fold area vs. crease length extracted from nine-perimeter folds, fit to the equations in (*E*). The resulting fit predicts a fold angle of ~45°. See *SI Appendix* for further discussion. Circle size represents crease length. Color represents fold identity. (*K*) Quantification of twist tightness. A single twist within a given animal can exhibit variable widths, as thin as 10 μm (on the order of a single cell diameter). (*L*) Summary schematic of motif-specific unfolding pathways. Motif dynamics arise from ciliary activity of the adjacent substrate-adherent patches (F_C). Motif-specific features, such as self-adhesion within hairpin folds (F_{CC}) and topology of a 2π twist lead to distinct dynamics, as highlighted in (*F*). [Scale bars: (*B*) 200 μm and (*C* and *D*) 100 μm.]

solitons or "twistons" as observed in graphene nanoribbons (37). Both 2π and -2π twists are observed to form in the same animal, enabling twist annihilation (twists colliding and resolving) and pile-up (twists colliding and stacking), depending on twist chirality (*SI Appendix*, Fig. S1). Furthermore, single twists can only be removed via transport to the animal's perimeter, whereas folds can be removed locally (Fig. 3 *B* and *C*). Twist geometries have been described in a variety of contexts (36, 39–42), but the effect of twists on epithelia has not been considered.

In summary, unfolding behavior sees the emergence of distinct motifs, each with particular resolution trajectories. Fig. 3*L* summarizes the basic physics underlying these trajectories. In all cases, ciliary forces generated by substrate-adherent tissue patches adjacent to the motif drive motif evolution. Self-adhesion forces within the hairpin fold and topology of the 2π twist lead to distinct curvature evolution pathways (seen in Fig. 3 *F* and *G*) and resolution outcomes, respectively. For example, opposing ciliary forces from motif-adjacent patches promote motif resolution in rucks and folds but yield tightening and sometimes rupture in 2π twists (Movie S8). Thus, the universal forcing mechanism of active ciliary patches produces different outcomes depending on the motif at hand.

Dynamics of Folded-Flat Transition. How an aneural organism coordinates a complex transition from a 3D folded to a flat state at the scale of an entire animal is not obvious. Moreover, the coordination of a ciliary carpet to manage folding/unfolding behavior is not a trivial task. To test the robustness of unfolding behavior and quantify unfolding pathways, we collected 163 unfolding time lapses (on flat substrates) from repeated trials across 45 animals (Fig. 4 *A* and *C* and Movie S9). This dataset reveals unfolding behavior to be extremely robust; all trials resulted in the animal reaching a final flattened state, except for one which ended in animal fission at the site of a twist (Movie S8). Furthermore, these time-lapse datasets reveal the extent of nonstereotypy in this process; each animal passes through a series of distinct folding intermediates along different trajectories before eventually reaching a flat state (Fig. 4*B* and *SI Appendix*, Fig. S1). Importantly, this is also the case for individual animals across repeated unfolding trials, indicating that the unfolding trajectory emerges from initial condition and stochastic activity, rather than being preprogrammed in the animal's physiology (*SI Appendix*, Fig. S2).

It is well known that *T. adhaerens* exhibits natural variation in body size and shape (24). Yet, how variation in animal size impacts unfolding behavior is not obvious. Using a mixture of small ($\lesssim 0.1\,\mathrm{mm}^2$) and large ($\gtrsim 1\,\mathrm{mm}^2$) animals (varying by roughly one order of magnitude in area), we performed ten repeated unfolding trials across ten animals (100 total measurements) (Fig. 4*D*). We find that, on average, large animals are roughly three times slower to unfold compared to small animals, likely due to their ability to configure into more complex folding states (Fig. 4 *E* and *F*) (43). Additionally, organizing unfolding times based on animal identity reveals a distribution of unfolding times in repeated trials, particularly for larger animals, which correspond to variations in unfolding paths taken (Fig. 4*E*). Thus, unfolding behavior does not have a fixed timescale, but rather proceeds as a function of the complexity of the folding state.

As with size, animal shape has the potential to impact unfolding behavior, as shape changes the pattern of active ciliary domains in contact with substrate. To test the impact of animal shape on unfolding, we performed unfolding trials for both toroidal and high-aspect ratio string-like animals (24). We find that toroidal animals are capable of complete unfolding despite their topologically distinct body plan (Fig. 4*J* and Movie S10). Interestingly, high-aspect-ratio animals also exhibit extensive unfolding (Fig. 4*J* and Movie S11), but twist defects tend to persist in the body (Fig. 4*J*, arrows), often leading to binary fission of the animal. These findings highlight the general and distributed nature of unfolding behavior, which can be realized in a wide range of body morphologies rather than requiring a specific body architecture.

Finally, previous work has demonstrated the role of the animal's ventral ciliary carpet, which exhibits characteristic collective dynamics, in driving locomotion (20, 23). Individual cilia exhibit a unique walking gait on a rigid substrate which, through local mechanical coupling, leads to the emergence of ciliary coherence on long length scales (20, 23). Our findings showed that interaction with a substrate is necessary for unfolding to occur (Fig. 4*C*). Thus, we tested whether normal ciliary activity is necessary for unfolding behavior by performing unfolding trials in calcium-free seawater (CFSW) or lithium chloride, both of which have been previously shown to perturb normal ciliary beating in *T. adhaerens* (44, 45) (Fig. 4 *G* and *H*, *SI Appendix*, Fig. S1, Movie S12, and *Materials and Methods*). We find that both treatments reversibly inhibit unfolding, demonstrating the critical driving role of ciliary activity in unfolding behavior. Cilia-resolved imaging also revealed ciliary activity proximal to folds and twists, making clear the fundamental role of cilia in this process (Movies S7 and S13). In addition, we tested the effects of CFSW and LiCl on folded-nonconforming animals and found that, relative to ASW, these conditions reduced local tissue motion, hinting at the role of cilia in the suspended animal's 3D shape dynamics (Movie S14). However, these dynamics are not sufficient to drive unfolding in the absence of a substrate.

Scaling Analysis of Cilia-Driven Folding–Unfolding. The physics of passive thin-sheet folding and deformation has been studied in a variety of contexts (27, 28, 31, 34, 46–52), including substrate delamination (34, 52), elastic wrinkling (28, 49), paper crumpling (53), and paper unfolding (48). Uniquely in the case of living self-folding sheets such as *T. adhaerens*, we must also account for the dynamics of distributed ciliary activity which injects energy into the system at the micron length scale. Cilia can be traced back to the last eukaryotic common ancestor (54, 55). However, ciliary activity and adhesion have not been previously implicated in epithelial folding processes. Here, we present a scaling-based approach to account for the contribution of collective ciliary activity to unfolding behavior.

To understand where *T. adhaerens* resides in the phase space of active folding, we consider a 1D folded sheet with length L, thickness t, fold width λ and fold height h (34, 52). The strain in this system ϵ is given by the length of excess material that has been absorbed into the fold, $\Delta = L - L'$. We define the relevant energy scales in the problem as 1) E_{bend} (out-of-plane bending energy), 2) $E_{tensile}$ (in-plane elastic energy), 3) $E_{cilia:substrate}$ (adhesion energy between the cilia layer and the substrate, abbreviated as E_{cs}), and 4) $E_{activity}$ (energy injected by ciliary walking). Leveraging past measurements of the bending modulus $B \sim 2 \times 10^{-13}\ \mathrm{N \cdot m}$ and Young's modulus $Et \sim 1.5 \times 10^{-2}\ \mathrm{N/m}$ in generic thin epithelial sheets (50), we evaluate the Föppel-von Kármán number $\gamma = YL^2/B \sim 7 \times 10^4$, which is much larger than 1 (see *Materials and Methods* and *SI Appendix* for details). Thus, out-of-plane bending is the preferred mechanism for releasing in-plane stress, which clearly points to the ready formation of folds in the system

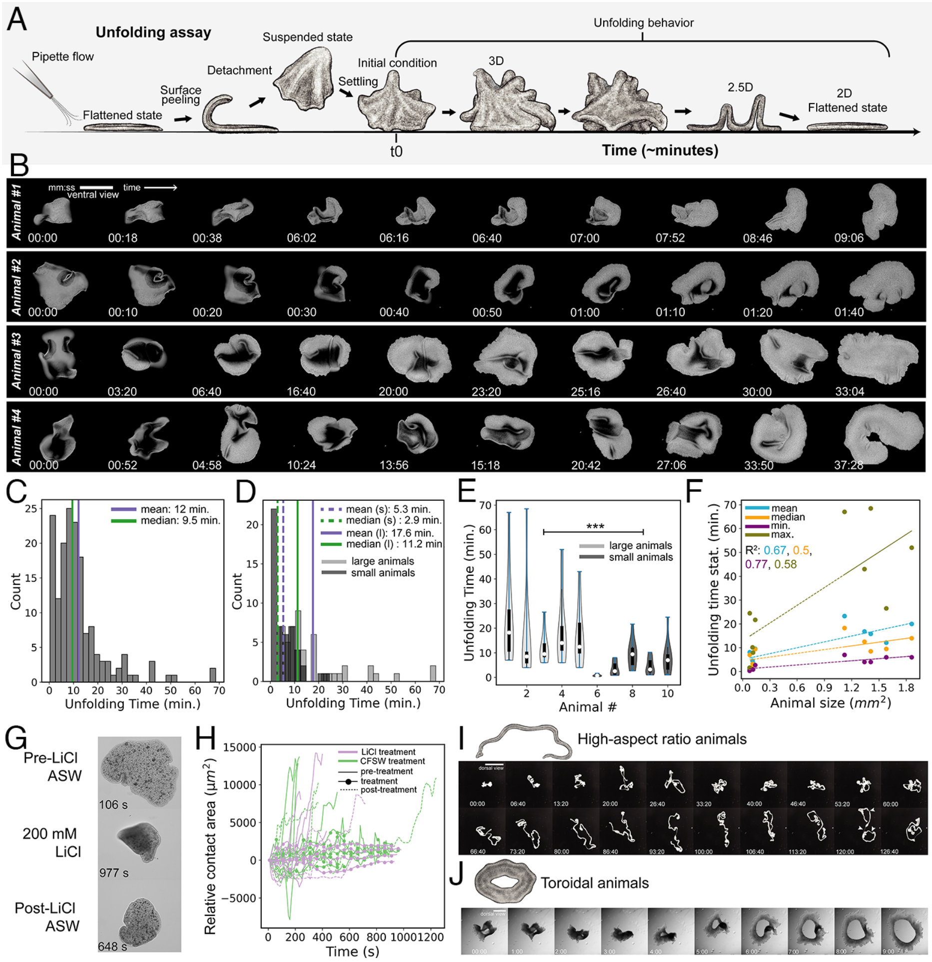

Fig. 4. Robustness, nonstereotypy, and timescales of unfolding behavior. (*A*) Schematic of the experimental assay used for studying unfolding behavior. Gentle flow from a pipette pushes the animal from a flat-conforming state to folded-nonconforming, triggering the onset of unfolding behavior. See *Materials and Methods*. (*B*) Example unfolding trials shown for four different animals, ventral view. Variation in initial folding state and timestamps highlight the nonstereotypy inherent to this process. (*C*) Histogram of *T. adhaerens* unfolding times for 163 trials across 45 animals demonstrating the robustness of the unfolding algorithm. We measure a mean unfolding time of 12 min and median unfolding time of 9.5 min. (*D*) Subset of data (100 trials) shown in (*C*) organized by animal size. Large animals ($\gtrsim$1 mm^2, light gray) consistently take longer to unfold than smaller animals ($\lesssim$0.1 mm^2, dark gray). (*E*) Distribution of unfolding times in (*D*) sorted by animal identity (labeled 1 to 10). Individual animals exhibit a wide range of unfolding times across repeated trials, and larger animals take significantly longer to unfold than smaller animals (Welch's $t(61.07) = 5.41, P = 1.08e-06$). (*F*) Positive correlation between mean ($R^2 = 0.67$), median ($R^2 = 0.5$), minimum ($R^2 = 0.77$), and maximum ($R^2 = 0.58$) unfolding times and animal size, further demonstrating the impact of animal size on unfolding time. (*G* and *H*) Treatment of animals with calcium-free sea water or 200 mM lithium chloride reversibly inhibits unfolding, as visualized through total animal–substrate contact area. Pretreatment, treatment, and posttreatment unfolding trials are shown for each individual animal. (*I* and *J*) Animals exhibiting atypical morphologies are still capable of unfolding, highlighting the general and distributed nature of the animal's unfolding algorithm. This can be seen for ultralong (~0.5 cm), string-like animals in (*I*) and toroidal animals in (*J*). [Scale bars: (*B* and *J*) 500 μm and (*I*) 2 mm.]

(Figs. 1–4). Additionally, we can write the total energy in the system as $E_{total} = E_{bend} + E_{tensile} + E_{cs} + E_{activity}$. $E_{cs} = F_{cs}\rho_c\lambda l_c$, where F_{cs} is the adhesion energy per cilium, ρ_c is the ciliary density, and l_c is the ciliary length; $E_{bend} = Et^3h^2/\lambda^3$; $E_{tensile} = Et^3\epsilon^2L$, where $\epsilon = \Delta/L$; and $E_{activity} = F_c\rho_c\epsilon L^2$, where F_c is the force exerted by a walking cilium. Using the above values for E_{bend} and $E_{tensile}$ (50); previous measurements of cilia–substrate adhesion $F_{cs} \sim 2\,nN/\text{cilium}$ (56); previous estimates of active ciliary force $F_c \sim 10\,\text{pN}$ (57, 58); and measurements of ciliary density $\rho_c \sim 0.4\,\text{cilia}/\mu\text{m}$ (*Materials and Methods*), we evaluate $\alpha = E_{bend}/E_{activity} \sim 0.158$, $\beta = E_{tensile}/E_{activity} \sim 0.06$, and $\gamma = E_{cs}/E_{activity} \sim 2.17$ (see *SI Appendix* for details). Thus, active ciliary forces dominate over elastic forces, permitting the emergence of folds as a function of local ciliary activity. Ciliary adhesive and active forces are comparable in magnitude, but because active forces scale with L (which can be large or small) and adhesive forces scale with λ (which is often relatively small and invariant), unfolding behavior is largely driven by active rather than passive properties of the sheet. Notably, this theoretical framework predicts that curtailing ciliary activity should inhibit unfolding behavior, which we indeed observed through LiCl and CFSW perturbations presented above (Fig. 4 *G* and *H* and Movie S12).

1D Toy Model of Active Folding and Unfolding. While scaling-based analysis demonstrates the potential of a ciliary collective to dominate over passive elastic properties of the body and drive unfolding; how that ciliary collective coordinates efficiently to yield robust unfolding behavior remains unknown. Thus, we develop a 1D toy model to explore how spatially organized stochastic ciliary activity can facilitate the folding–unfolding transition (Fig. 5 and *SI Appendix*, Fig. S3, see *SI Appendix* for further details).

We consider a string of cells with in-plane stiffness $E_{tensile}$, bending modulus E_{bend}, surface adhesion E_{cs}, ciliary activity F_c (see *SI Appendix* for details), and self-adhesion E_{cc}, which repre-

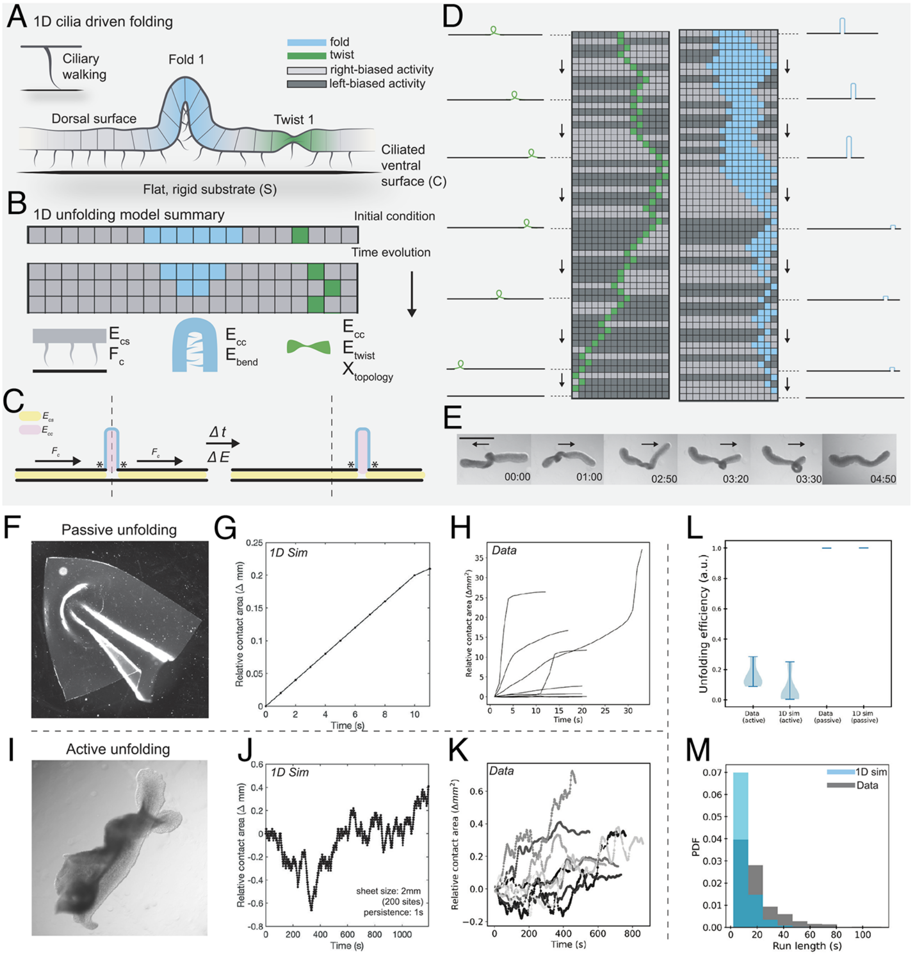

Fig. 5. 1D Toy model of active folding and unfolding. (*A*) We consider the energetics of active folding and unfolding in a 1D context. (*B*) We develop a 1D toy model of *T. adhaerens* to capture the time evolution of hairpin folds, twists, and active flat domains in a 1D lattice. Self-adhesion energy E_{CC} is associated with folds (cyan) and twists (green), while substrate adhesion energy E_{CS} is associated with flat regions (gray). Directional activity of flat regions biases the motion of fold and twist boundaries to the *Right* (light gray) or *Left* (dark gray). See *SI Appendix* for model details. (*C*) At each time step in the simulation, the *Left* and *Right* junctions of the fold or twist (marked with an asterisk) are perturbed in all possible directions, and the lowest energy perturbation is selected for the folding state at the next time step. (*D*) Example simulations of a single twist (*Left*, shown in green) and fold (*Right*, shown in cyan). Columns indicate lattice sites and rows indicate the lattice state over time. In both cases, patch activity leads to the removal of the motif through random switching of directional activity. (*E*) Example of a twisted animal demonstrating directional switching of ciliary patches. Initially, the twist moves to the *Left*, but reorientation of the cilia ultimately moves the twist to the *Right*. (Scale bar: 500 μm.) (*F*) To represent a case of passive unfolding, we collected unfolding time lapses of silicone rubber sheets on in a glass dish with a layer of silicone oil. In this system without activity, our toy model predicts (*G*) a linear increase in contact area over time as folded sites are converted to flat sites. (*H*) Indeed, we observe linear increases in contact area over time as the system unfolds. In contrast, (*I*) *T. adhaerens* presents a case of active unfolding. (*J*) With random ciliary activity, our toy model predicts fluctuations in contact area, as ciliary patches bias the process of folding and unfolding. Trajectory shown for a 2 mm lattice (200 sites), with a 1 s activity persistence time and 100 μm fold (20 sites). (*K*) Extracting contact area over time for ten unfolding animals reveals fluctuations in contact area. (*L*) Unfolding efficiency, defined as $\frac{A_N - A_1}{\sum_{i=1}^{N} |\Delta A_i|}$, for the unfolding trajectories shown in panels (*G*, *H*, *J*, and *K*). (*M*) Distribution of run lengths in active simulations and *T. adhaerens* unfolding data, where run length is the duration of time a system spends increasing or decreasing contact area without reversal.

sents the adhesion energy between a pair of cilia in contact within a hairpin fold (*Materials and Methods* and *SI Appendix*, Fig. S5 *A* and *B*). The behavior of this string is determined by a competition between E_{cs}, E_{cc}, and F_c (Fig. 5 *B* and *C*). At each simulation time step, ΔE_{total} (the change in total system energy) is calculated for all possible positional perturbations of the fold boundaries and the resulting lowest-energy perturbation is chosen for the evolved folding state (*Materials and Methods* and Fig. 5 *C* and *D*).

For simplicity, we consider how such a discrete sheet behaves with hairpin folds and 2π twists (Fig. 5*B*). In the passive case ($F_c = 0$), folding or unfolding occurs based on the ratio E_{cs}/E_{cc} (*SI Appendix*, Fig. S3). When ($F_c > 0$), active forces (arising from flat regions of the lattice) can directly influence the folding state (*SI Appendix*, Fig. S3). We assign activity a "persistence time," defined as the timescale on which a patch is oriented in a particular direction (i.e. *Left* or *Right*) before randomly reorienting. Fig. 5*E* shows an example of these reorientation dynamics in our data, where a twist is first observed moving to the *Left* before it ultimately moves to the *Right* as a result of ciliary reorientation (also seen in Movie S7). By comparing distributions of run lengths for simulation and experimental data (defined as the durations of periods within unfolding trajectories which display monotonic increases or decreases in contact area), we see the effects of ciliary persistence time in simulation vs. data (Fig. 5*M*). Differences in these two distributions likely result from two factors, namely the greater diversity of folding states present in the data as compared to simulation; and the difference in dimensionality (activity dynamics simulated in 1D cannot fully capture the collective ciliary dynamics in 2D).

Using this toy model, we compare and contrast passive folding with active folding. For an initial condition with a single central fold, zero patch activity will result in a monotonic increase in contact area as the fold is removed (Fig. 5*G*). To test these conditions experimentally, we performed unfolding assays with silicone rubber sheets on a glass substrate lubricated with silicone oil (Fig. 5*F*). Indeed, these passive sheets unfold without fluctuations in contact area, instead showing a monotonic increase in their contact area with the glass substrate (Fig. 5*H*). In contrast, a nonzero patch activity will result in nonmonotonic increase in contact area, with fluctuations as patch activity randomly reorients according to the cilia persistence time (Fig. 5*J*). Experimentally, we extracted the contact area from unfolding *T. adhaerens* and also observe substantial nonmonotonic fluctuation in contact area before eventual unfolding occurs (Fig. 5*K*). To quantify this effect, we introduce an unfolding efficiency metric, defined as $\frac{A_N - A_1}{\sum_{i=1}^{N} |\Delta A_i|}$, which compares the total cumulative distance ($\sum_{i=1}^{N} |\Delta A_i|$) of an unfolding trajectory over duration $N\Delta t$, to the difference between the final and initial contact area ($A_N - A_1$), showing a stark difference between the active vs. passive cases (Fig. 5*L*). Thus, the observed fluctuation in contact area over time is a signature of unfolding driven by stochastic distributed activity.

A

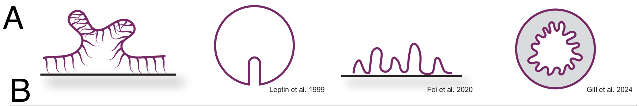

B

	T. adhaerens	*D. melanogaster*	*V. cholerae*	*G. domesticus*
fold context	animal behavior	animal development (ventral furrow)	bacterial biofilm wrinkling	animal development (gut wrinkling)
activity source	animal motility	cell shape change	cell growth	cell growth
activity mechanism	ciliary walking/ substrate adhesion	actomyosin contractility	nonuniform cell growth/ substrate friction	differential cell growth/ tissue strain mismatch
substrate	external environment (glass surface)	None	external environment (agar surface)	gut mesenchyme
stereotyped	no	yes	no	no
reversible	yes	no	no	no
folding timescale	seconds - minutes	15-30 minutes	hours - days	5-10 days
folding height	~10-100 μm	~30 μm Royou et al. 2004	~10-100 μm	~10-100 μm
folding path	(Folding/Unfolding efficiency) << 1	~ 1	~ 1	~ 1

Fig. 6. *T. adhaerens* folding in context. (*A*) Comparison of *T. adhaerens* folding behavior with other examples of epithelial folding in living systems, including the development of the ventral furrow in the *Drosophila* embryo (62, 63); the formation of wrinkles in *V. cholerae* biofilms (64); and the emergence of folds in the chick gut lining (65). (*B*) *T. adhaerens* offers a mechanism for thin-sheet folding, differing from other systems in its fast timescale, reversibility, and stochastic activity leading to a low folding/unfolding efficiency (as defined above).

Discussion

Our finding of a cilia-driven folding and unfolding behavior establishes *T. adhaerens* as a tractable living system for studying the mechanics of thin-sheet folding driven by distributed cellular activity. Future studies will examine the relationship between biochemical signals and sheet mechanics in *T. adhaerens*. For example, neuropeptides are known to trigger folding in *T. adhaerens* on flat substrates (59), but the interplay between neuropeptide response and modulation of cellular activity to trigger folding remains to be understood. Additionally, the high curvatures observed in folds (Fig. 2*B*) raise the question of cellular curvature sensing within *T. adhaerens*. It has been shown that epithelial sheets exhibit fast response to curvature (60), but few studies have been done to test the response to dynamically modulating curvature due to a lack of model systems (61). *T. adhaerens* is a powerful model system for studying dynamic epithelial curvature response.

It is useful to compare *T. adhaerens* folding–unfolding behavior with other biological examples of active folding and wrinkling. Fig. 6 provides qualitative and quantitative comparisons with ventral furrow development in the *Drosophila* embryo (62, 63), wrinkling in *Vibrio cholerae* biofilms (64), and folding in the chick gut lining (65). In all four cases, wrinkling or folding emerges from active cellular processes such as cell growth, shape change, or motility. *T. adhaerens* presents a unique case of folding emerging from behavior, specifically animal-scale ciliary motility. The reversible and stochastic nature of this motility leads to a low unfolding efficiency, a feature which is absent from the other systems. Moreover, while all four cases exhibit folds on comparable length scales, *T. adhaerens* exhibits nonstereotyped, reversible folding on much shorter time scales, making it a rich system for studying folding–unfolding dynamics. These unique qualities position *T. adhaerens* as a valuable model system for investigating the mechanics of epithelial folding.

Our work demonstrates that ciliary activity (coupled to a rigid substrate boundary condition) is able to drive epithelial folding and unfolding without genetic control. Other examples of emergent mechanical folding have been recently noted in developmental systems (66, 67). It is possible that even before the evolution of molecular-driven epithelial folding processes, like those studied in embryonic development, a multitude of other active cellular mechanisms (e.g. ciliary activity, flagellar beating, substrate adhesion, contractility, etc.) enabled epithelial folding, perhaps allowing primitive multicellular organisms to achieve dynamic three-dimensional forms (15). Given that the earliest animals possessed cilia (54), ciliary interactions with environmental substrates may have enabled epithelial folding in early animals. More broadly, our work shows the importance of environmental geometry in shaping the morphology of soft-bodied, surface-adherent organisms.

Our measurements of inner-fold width and ciliary length reveal a configuration of interciliary contact within folds (Fig. 2*D*). Combining these measurements with cilia-resolved imaging (*SI Appendix*, Fig. S1), we establish the presence of direct physical interciliary interaction within folds. Interciliary interactions have been studied in a variety of contexts, including hydrodynamic synchronization (68) and ciliate mating (69). Here, we present a unique geometry enabling the interaction between two parallel, open-facing regions of a single animal's ciliary carpet, inviting future study into the possible hydrodynamic and biochemical modes of communication at play within ciliated folds.

The general phenomenon of folding driven by a combination of cell activity, surface adhesion, and substrate geometry is relevant to understanding the physics of development. Recent work has begun to highlight the role of cellular interaction with the extraembryonic boundary in developing embryos (70). However, more studies are needed to explore the effects of embryonic-boundary interactions on epithelial folding and other morphogenic processes. Similarly, in organoid growth, morphogenesis often occurs on a substrate. Yet, we have a limited understanding of how interactions with this substrate, or the geometry of this substrate, impacts morphogenesis. Previous work has established the importance of substrate nanotopography in organoid growth (71). However, the role of mesoscale substrate geometry has not been considered. Our study demonstrates the capacity of epithelia–substrate interactions for driving morphological change, and invites further investigation into similar processes in developing embryos and organoids.

Our finding of folded placozoan morphotypes guided by substrate geometry provides insight into the ecophysiology of *T. adhaerens*, particularly with respect to feeding, dispersal, and response to turbulence in the ocean (*SI Appendix*, Fig. S8). Previous work has shown that *T. adhaerens* feeds in a flat-conforming state by "grazing" on algal lawns, secreting digestive enzymes via the ventral epithelium to lyse algal cells before uptaking nutrients (72). Our work identifies a second feeding modality in which the animal conforms to globular algal clusters, adopting a folded-conforming state guided by algal geometry (Fig. 1*C* and Movie S4). Folding during feeding may alter how digestive enzymes are spatially distributed, potentially localizing nutrient uptake to specific regions of the body. Further studies are needed to explore the physiological implications of fold geometry on feeding mechanisms.

The identification of folded-conforming animals on algal substrates suggests a broader range of possible food sources available to *T. adhaerens* in the ocean, including free-floating algal aggregates in the water column rather than being limited to benthic substrates in the intertidal zone. Previous environmental sampling efforts have focused on collecting placozoans from stones and corals in shallow waters, but the animals have also been isolated from the water column, implying the existence of a planktonic state (73, 74). In this surface-detached state, folding may offer advantages such as reduced hydrodynamic drag and protection of the ventral epithelium. In addition, the ability to conform to free-floating food links feeding with dispersal, as *T. adhaerens* may hitch rides on colonial or aggregate algae and travel in the planktonic state with food on hand. Such a strategy is advantageous due to the scarcity of food in the water column at the microbial scale.

The ability to rapidly and robustly transition between folded and flattened states is likely critical for *T. adhaerens'* survival in the ocean, where patchy, turbulent flows in shallow waters can lead to surface detachment. Substrate detachment can be triggered by neuropeptide signaling, raising the possibility that placozoans actively regulate when to leave substrates in response to chemical, physical, or social cues (59). In this context, the capability to unfold and reattach efficiently is essential for maintaining control over habitat and food access.

It is interesting to consider the range of parameters explored by evolution to produce robust folding–unfolding behavior in this simple animal. Slight variations in morphological parameters such as ciliary adhesion, activity, animal size, and bending modulus would render folding–unfolding behavior impossible. For example, stronger ciliary adhesion would lead to stuck states and prevent ciliary walking necessary for locomotion and unfolding. Similarly, weaker ciliary activity would lead to fold maintenance, as ciliary collectives would not be able to provide enough force to remove folds. Instead, evolution has produced a robust solution for thin-sheet folding and unfolding in the physiology of *T. adhaerens*. Future work is needed to understand the mechanisms by which the animal's ciliary collective coordinates the resolution of complex folding states. Previous studies have highlighted the role of mechanics in ciliary coordination, as individual cilia exert torques on their neighbors, leading to coherent locomotion (20, 23). Yet, how this aneural mechanical process is capable of efficiently and robustly solving folding problems remains to be understood.

We expect this finding of living, multicellular active folding to inspire a class of engineered living and nonliving active folding processes, which rely on local, distributed activity to drive surface-attached unfolding. Self-folding has proven to be a powerful tool in engineering to build a variety of deployable structures, including telescope sunshields (75), soft robots (76, 77), and microscale devices (78). Our work highlights a robust algorithm for active epithelial folding and unfolding in a simple animal.

Conclusions

In conclusion, we have identified a folding–unfolding behavior exhibited by the early diverging animal *T. adhaerens*. This nonstereotyped behavior is governed by local substrate geometry and the active–adhesive interaction between the animal's ventral ciliary carpet and a rigid substrate. Our work highlights the vast configuration space of active thin-sheet folding beyond what is typically seen in developmental epithelial folding. Through experiments, scaling analysis, and toy modeling, we show that *T. adhaerens* undergoes reversible, nonstereotyped folding–unfolding transitions driven by ciliary activity. Our finding of distributed active unfolding behavior lays the groundwork for engineering a class of active origami materials; motivates further consideration of the substrate in epithelial folding processes; and reveals possible folding morphodynamics of early epithelia.

Materials and Methods

Detailed methods are provided in *SI Appendix*.

Data, Materials, and Software Availability. The code used for simulation is available on GitHub (https://github.com/charlottebrannon/1D-active-folding-unfolding.git) (79). The data that support the findings within this study are available on Dryad (https://doi.org/10.5061/dryad.xpnvx0kvd) (80).

ACKNOWLEDGMENTS. We thank all members of the Prakash Lab for helpful discussions. We thank Rebecca Konte for assistance with figure art and design. We thank Hongquan Li for SQUID-based tracking microscopes. We thank the Stanford Cell Science Imaging Facility. C.M.B. acknowledges funding support from the NIH/National Institute of General Medical Sciences Cell and Molecular Biology Training Grant (5T32GM007276) and the NSF Graduate Research Fellowship Program. M.P. acknowledges financial support from Schmidt Futures Innovation Fellowship, Moore Foundation, Dalio Foundation, NSF Center for Cellular Construction, NSF Growing Convergence Research Grant, and Woods Institute for the Environment.

Author affiliations: [a]Department of Biology, Stanford University, Stanford, CA 94305; [b]Department of Bioengineering, Stanford University, Stanford, CA 94305; [c]Woods Institute for the Environment, Stanford University, Stanford, CA 94305; and [d]Oceans Department, Stanford University, Stanford, CA 94305

1. L. Sui *et al.*, Differential lateral and basal tension drive folding of *Drosophila* wing discs through two distinct mechanisms. *Nat. Commun.* **9**, 4620 (2018).
2. S. K. Akula, D. Exposito-Alonso, C. A. Walsh, Shaping the brain: The emergence of cortical structure and folding. *Dev. Cell* **58**, 2836–2849 (2023).
3. E. Nikolopoulou, G. L. Galea, A. Rolo, N. D. E. Greene, A. J. Copp, Neural tube closure: Cellular, molecular and biomechanical mechanisms. *Development* **144**, 552–566 (2017), https://journals.biologists.com/dev/article-pdf/144/4/552/3431148/dev145904.pdf.
4. V. Conte *et al.*, A biomechanical analysis of ventral furrow formation in the *Drosophila melanogaster* embryo. *PLoS One* **7**, 1–17 (2012).
5. G. Odell, G. Oster, P. Alberch, B. Burnside, The mechanical basis of morphogenesis: I. Epithelial folding and invagination. *Dev. Biol.* **85**, 446–462 (1981).
6. R. E. Dawes-Hoang *et al.*, folded gastrulation, cell shape change and the control of myosin localization. *Development* **132**, 4165–4178 (2005).
7. A. C. Martin, B. Goldstein, Apical constriction: Themes and variations on a cellular mechanism driving morphogenesis. *Development* **141**, 1987–1998 (2014).
8. M. Tozluo-lu *et al.*, Planar differential growth rates initiate precise fold positions in complex epithelia. *Dev. Cell* **51**, 299–312.e4 (2019).
9. T. Savin *et al.*, On the growth and form of the gut. *Nature* **476**, 57–62 (2011).
10. J. J. Zartman, S. Y. Shvartsman, Unit operations of tissue development: Epithelial folding. *Annu. Rev. Chem. Biomol. Eng.* **1**, 231–246, PMID: 22432580 (2010).
11. L. Wang *et al.*, Tmem161b modulates radial glial scaffolding in neocortical development. *Proc. Natl. Acad. Sci. U.S.A.* **120**, e2209983120 (2023).
12. E. R. Detrait *et al.*, Human neural tube defects: Developmental biology, epidemiology, and genetics. *Neurotoxicol. Teratol.* **27**, 515–524 (2005).
13. D. A. Matoz-Fernandez, F. A. Davidson, N. R. Stanley-Wall, R. Sknepnek, Wrinkle patterns in active viscoelastic thin sheets. *Phys. Rev. Res.* **2**, 013165 (2020).
14. C. Fei *et al.*, Nonuniform growth and surface friction determine bacterial biofilm morphology on soft substrates. *Proc. Natl. Acad. Sci. U.S.A.* **117**, 7622–7632 (2020).
15. T. Brunet *et al.*, Light-regulated collective contractility in a multicellular choanoflagellate. *Science* **366**, 326–334 (2019).
16. S. Höhn, A. R. Honerkamp-Smith, P. A. Haas, P. K. Trong, R. E. Goldstein, Dynamics of a volvox embryo turning itself inside out. *Phys. Rev. Lett.* **114**, 178101 (2015).
17. M. Olivetta, C. Bhickta, N. Chiaruttini, J. Burns, O. Dudin, A multicellular developmental program in a close animal relative. *Nature* **635**, 382–389 (2024).
18. S. R. Najle *et al.*, Stepwise emergence of the neuronal gene expression program in early animal evolution. *Cell* **186**, 4676–4693.e29 (2023).
19. C. L. Smith *et al.*, Novel cell types, neurosecretory cells, and body plan of the early-diverging metazoan *Trichoplax adhaerens*. *Curr. Biol.* **24**, 1565–1572 (2014).
20. M. S. Bull, V. N. Prakash, M. Prakash, Ciliary flocking and emergent instabilities enable collective agility in a non-neuromuscular animal. arXiv [Preprint] (2021). https://arxiv.org/pdf/2107.02934 (Accessed 1 September 2024).
21. T. D. Mayorova, K. Hammar, C. A. Winters, T. S. Reese, C. L. Smith, The ventral epithelium of *Trichoplax adhaerens* deploys in distinct patterns cells that secrete digestive enzymes, mucus or diverse neuropeptides. *Biol. Open* **8**, bio045674 (2019).
22. M. S. Bull, M. Prakash, Mobile defects born from an energy cascade shape the locomotive behavior of a headless animal. arXiv [Preprint] (2021). https://arxiv.org/pdf/2107.02940 (Accessed 1 September 2024).
23. M. S. Bull, L. A. Kroo, M. Prakash, Excitable mechanics embodied in a walking cilium. arXiv [Preprint] (2021). https://arxiv.org/pdf/2107.02930 (Accessed 1 September 2024).
24. V. N. Prakash, M. S. Bull, M. Prakash, Motility-induced fracture reveals a ductile-to-brittle crossover in a simple animal's epithelia. *Nat. Phys.* **17**, 504–511 (2021).
25. S. Armon, M. S. Bull, A. Aranda-Diaz, M. Prakash, Ultrafast epithelial contractions provide insights into contraction speed limits and tissue integrity. *Proc. Natl. Acad. Sci. U.S.A.* **115**, E10333–E10341 (2018).
26. D. Krishnamurthy *et al.*, Scale-free vertical tracking microscopy. *Nat. Methods* **17**, 1040–1051 (2020).
27. S. Liu *et al.*, Conformability of flexible sheets on spherical surfaces. *Sci. Adv.* **9**, eadf2709 (2023).
28. Q. Wang, X. Zhao, A three-dimensional phase diagram of growth-induced surface instabilities. *Sci. Rep.* **5**, 8887 (2015).
29. D. L. Blair, A. Kudrolli, Geometry of crumpled paper. *Phys. Rev. Lett.* **94**, 166107 (2005).
30. A. D. Cambou, N. Menon, Three-dimensional structure of a sheet crumpled into a ball. *Proc. Natl. Acad. Sci. U.S.A.* **108**, 14741–14745 (2011).
31. H. Aharoni, E. Sharon, Direct observation of the temporal and spatial dynamics during crumpling. *Nat. Mater.* **9**, 993–997 (2010).
32. Y. C. Lin *et al.*, Spontaneous emergence of ordered phases in crumpled sheets. *Phys. Rev. Lett.* **103**, 263902 (2009).
33. S. B. Lemke, C. M. Nelson, Dynamic changes in epithelial cell packing during tissue morphogenesis. *Curr. Biol.* **31**, R1098–R1110 (2021).
34. B. Davidovitch, V. Démery, Rucks and folds: Delamination from a flat rigid substrate under uniaxial compression. *Eur. Phys. J. E* **44**, 11 (2021).
35. J. M. Kolinski, P. Aussillous, L. Mahadevan, Shape and motion of a ruck in a rug. *Phys. Rev. Lett.* **103**, 174302 (2009).
36. J. Chopin, A. Kudrolli, Tensional twist-folding of sheets into multilayered scrolled yarns. *Sci. Adv.* **8**, eabi8818 (2022).
37. A. V. Savin, E. A. Korznikova, S. V. Dmitriev, Twistons in graphene nanoribbons on a substrate. *Phys. Rev. B* **102**, 245432 (2020).
38. S. Vafaei, M. Podowski, Analysis of the relationship between liquid droplet size and contact angle. *Adv. Colloid Interface Sci.* **113**, 133–146 (2005).
39. J. Mu *et al.*, Sheath-run artificial muscles. *Science* **365**, 150–155 (2019).
40. K. Conley, L. Godbout, M. T. Whitehead, T. G. van de Ven, Origin of the twist of cellulosic materials. *Carbohydr. Polym.* **135**, 285–299 (2016).
41. H. C. Han, Twisted blood vessels: Symptoms, etiology and biomechanical mechanisms. *J. Vasc. Res.* **49**, 185–197 (2012).
42. Z. Chen, Q. Guo, E. Dai, N. Forsch, L. A. Taber, How the embryonic chick brain twists. *J. R. Soc. Interface* **13**, 20160395 (2016).
43. B. HAudoly, Y. Pomeau, *Elasticity and Geometry: From Hair Curls to the Nonlinear Response of Shells* (Oxford University Press, London, 2018).
44. J. Zuccolotto-Arellano, R. Cuervo-González, Binary fission in trichoplax is orthogonal to the subsequent division plane. *Mech. Dev.* **162**, 103608 (2020).
45. M. Leria *et al.*, Fast calcium-dependent reorientation of motile cilia basal bodies in the simple metazoan, Trichoplax. bioRxiv [Preprint] (2025). https://www.biorxiv.org/content/early/2025/08/25/2025.08.22.671430.full.pdf (Accessed 1 September 2025).
46. J. Andrejevic, L. M. Lee, S. M. Rubinstein, C. H. Rycroft, A model for the fragmentation kinetics of crumpled thin sheets. *Nat. Commun.* **12**, 1470 (2021).
47. O. Gottesman, J. Andrejevic, C. H. Rycroft, S. M. Rubinstein, A state variable for crumpled thin sheets. *Commun. Phys.* **1**, 70 (2018).
48. F. C. B. Leal, M. A. F. Gomes, Unfolding of crumpled thin sheets. *Phys. Rev. E* **106**, 025002 (2022).
49. F. Box *et al.*, Dynamics of wrinkling in ultrathin elastic sheets. *Proc. Natl. Acad. Sci. U.S.A.* **116**, 20875–20880 (2019).
50. J. Fouchard *et al.*, Curling of epithelial monolayers reveals coupling between active bending and tissue tension. *Proc. Natl. Acad. Sci. U.S.A.* **117**, 9377–9383 (2020).
51. A. B. Croll *et al.*, Sticky crumpled matter. *Matter* **5**, 1792–1805 (2022).
52. M. Kothari, Z. Lemon, C. Roth, T. Cohen, Controlled propagation and jamming of a delamination front. *Soft Matter* **16**, 9838–9843 (2020).
53. S. Deboeuf, E. Katzav, A. Boudaoud, D. Bonn, M. Adda-Bedia, Comparative study of crumpling and folding of thin sheets. *Phys. Rev. Lett.* **110**, 104301 (2013).
54. T. Cavalier-Smith, The phagotrophic origin of eukaryotes and phylogenetic classification of protozoa. *Int. J. Syst. Evol. Microbiol.* **52**, 297–354 (2002).
55. P. Satir, D. R. Mitchell, G. Jékely, "Chapter 3 how did the cilium evolve?" in *Ciliary Function in Mammalian Development, Volume 85 of Current Topics in Developmental Biology*, B. K. Yoder, Ed. (Academic Press, 2008), pp. 63–82.
56. C. T. Kreis, M. Le Blay, C. Linne, M. M. Makowski, O. Bäumchen, Adhesion of Chlamydomonas microalgae to surfaces is switchable by light. *Nat. Phys.* **14**, 45–49 (2018).
57. T. J. Böddeker, S. Karpitschka, C. T. Kreis, Q. Magdelaine, O. Bäumchen, Dynamic force measurements on swimming chlamydomonas cells using micropipette force sensors. *J. R. Soc. Interface* **17**, 20190580 (2020).
58. D. B. Hill *et al.*, Force generation and dynamics of individual cilia under external loading. *Biophys. J.* **98**, 57–66 (2010).
59. F. Varoqueaux *et al.*, High cell diversity and complex peptidergic signaling underlie placozoan behavior. *Curr. Biol.* **28**, 3495–3501.e2 (2018).
60. S. Blonski *et al.*, Direction of epithelial folding defines impact of mechanical forces on epithelial state. *Dev. Cell* **56**, 3222–3234.e6 (2021).
61. M. Luciano, C. Tomba, A. Roux, S. Gabriele, How multiscale curvature couples forces to cellular functions. *Nat. Rev. Phys.* **6**, 246–268 (2024).
62. M. Leptin, Gastrulation in *Drosophila*: The logic and the cellular mechanisms. *EMBO J.* **18**, 3187–3192 (1999).
63. A. Royou, C. Field, J. C. Sisson, W. Sullivan, R. Karess, Reassessing the role and dynamics of nonmuscle myosin II during furrow formation in early *Drosophila* embryos. *Mol. Biol. Cell* **15**, 838–850 (2004).
64. C. Fei *et al.*, Nonuniform growth and surface friction determine bacterial biofilm morphology on soft substrates. *Proc. Natl. Acad. Sci. U.S.A.* **117**, 7622–7632 (2020).
65. H. K. Gill *et al.*, The developmental mechanics of divergent buckling patterns in the chick gut. *Proc. Natl. Acad. Sci. U.S.A.* **121**, e2310992121 (2024).
66. B. C. Vellutini *et al.*, Patterned invagination prevents mechanical instability during gastrulation. *Nature* **646**, 627–636 (2025).
67. B. Dey *et al.*, Divergent evolutionary strategies pre-empt tissue collision in gastrulation. *Nature* **646**, 637–646 (2025).
68. A. Vilfan, F. Jülicher, Hydrodynamic flow patterns and synchronization of beating cilia. *Phys. Rev. Lett.* **96**, 058102 (2006).
69. T. Watanabe, "Chapter the role of ciliary surfaces in mating in paramecium" in *Ciliary and Flagellar Membranes*, R. A. Bloodgood, Ed. (Plenum Press, 1990), pp. 149–171.
70. S. Münster *et al.*, Attachment of the blastoderm to the vitelline envelope affects gastrulation of insects. *Nature* **568**, 395–399 (2019).
71. Y. Shen, Y. Hou, S. Yao, P. Huang, L. Yobas, In vitro epithelial organoid generation induced by substrate nanotopography. *Sci. Rep.* **5**, 9293 (2015).
72. C. L. Smith, N. Pivovarova, T. S. Reese, Coordinated feeding behavior in trichoplax, an animal without synapses. *PLoS One* **10**, 1–15 (2015).
73. M. Eitel, B. Schierwater, The phylogeography of the placozoa suggests a taxon-rich phylum in tropical and subtropical waters. *Mol. Ecol.* **19**, 2315–2327 (2010).
74. Y. K. Maruyama, Occurrence in the field of a long-term, year-round, stable population of placozoans. *Biol. Bull.* **206**, 55–60 (2004).
75. L. Wilson, S. Pellegrino, R. Danner, "Origami Sunshield Concepts for Space Telescopes" in *54th AIAA/ASME/ASCE/AHS/ASC Structures, Structural Dynamics, and Materials Conference*. (Boston, Massachusetts, 2013) https://doi.org/10.2514/6.2013-1594.
76. J. Li, H. Godaba, Z. Zhang, C. Foo, J. Zhu, A soft active origami robot. *Extrem. Mech. Lett.* **24**, 30–37 (2018).
77. R. K. Manna, A. Laskar, O. E. Shklyaev, A. C. Balazs, Harnessing the power of chemically active sheets in solution. *Nat. Rev. Phys.* **4**, 125–137 (2022).
78. Y. Zhu, M. Birla, K. R. Oldham, E. T. Filipov, Elastically and plastically foldable electrothermal micro-origami for controllable and rapid shape morphing. *Adv. Funct. Mater.* **30**, 2003741 (2020).
79. C. Brannon, 1D-active-folding-unfolding. GitHub. https://github.com/charlottebrannon/1D-active-folding-unfolding. Deposited 16 November 2025.
80. C. Brannon, M. Prakash, Dataset: Cilia-driven epithelial folding and unfolding in an early-diverging animal. Dryad. https://doi.org/10.5061/dryad.xpnvx0kvd. Deposited 14 November 2025.